Solar Energy Materials & Solar Cells 206 (2020) 110300

Contents lists available at ScienceDirect

Solar Energy Materials and Solar Cells

journal homepage: www.elsevier.com/locate/solmat

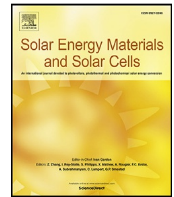

Impact of rough substrates on hydrogen-doped indium oxides for the application in CIGS devices

Darja Erfurt [a,*], Takashi Koida [b], Marc D. Heinemann [a], Chen Li [c,**,1], Tobias Bertram [a], Jiro Nishinaga [b], Bernd Szyszka [d], Hajime Shibata [b], Reiner Klenk [a], Rutger Schlatmann [a,e]

[a] PVcomB, Helmholtz-Zentrum Berlin für Materialien und Energie, Schwarzschildstr. 3, 12489 Berlin, Germany
[b] Research Center for Photovoltaics, National Institute of Advanced Industrial Science and Technology, 1-1-1 Umezono, Tsukuba 305-8568, Japan
[c] Stuttgart Center for Electron Microscopy, Max Planck Institute for Solid State Research, 70569 Stuttgart, Germany
[d] FG Technologie für Dünnschicht-Bauelemente, Technische Universität Berlin, Einsteinufer 25, 10587 Berlin, Germany
[e] Hochschule für Technik und Wirtschaft Berlin, Treskowallee 8, 10318 Berlin, Germany

ARTICLE INFO

Keywords:
High-mobility
Indium oxide
CIGS
Roughness
In_2O_3:H
Topography

ABSTRACT

Indium oxide based transparent conductive oxides (TCOs) are promising contact layers in solar cells due to their outstanding electrical and optical properties. However, when applied in Cu(In,Ga)Se_2 or Si-hetero-junction solar cells the specific roughness of the material beneath can affect the growth and the properties of the TCO. We investigated the electrical properties of hydrogen doped and hydrogen-tungsten co-doped indium oxides grown on rough Cu(In,Ga)Se_2 samples as well as on textured and planar glass. At sharp ridges and V-shaped valleys crack-shaped voids form inside the indium oxide films, which limit the effective electron mobility of the In_2O_3:H and In_2O_3:H,W thin films. This was found for films deposited by magnetron sputtering and reactive plasma deposition at several deposition parameters, before as well as after annealing and solid phase crystallization. This suggests universal behavior that will have a wide impact on solar cell devices.

1. Introduction

In recent years, researchers have shown an increased interest in high-mobility transparent conductive oxides (TCOs) for use in a wide range of applications, such as photovoltaics or displays. Due to high electron mobilities (μ_e) over 80 cm^2 V^{-1} s^{-1} and moderate charge carrier densities (n_e) around $1 \cdot 10^{20}$ cm^{-3} resistivities (ρ) below $1 \cdot 10^{-3}$ Ω cm are achieved. By this the free carrier absorption in the near infrared is minimized, leading to high transmittance. Previous studies reported about TCOs with electron mobilities above 80 cm^2 V^{-1} s^{-1} by doping In_2O_3 with H [1,2] and/or metals, such as W [3,4], Ce [3,5], Zr [6] or Mo [7]. The successful implementation as front contact was demonstrated for Si-heterojunction [6,8,9] and Cu(In,Ga)(S,Se)$_2$ (CIGS) [10,11] solar cells. In these solar cells, the TCO layers were deposited by physical vapor deposition at low temperatures, followed by postannealing at temperatures less than ≈ 200 °C. A phase transition from the amorphous to the polycrystalline state was confirmed during postannealing and the crystallized films show high electron mobility.

In general, CIGS photovoltaic devices show a high potential with a current world record cell efficiency of 23.35% on 1 cm^2 [12]. However, recently Bermudez et al. [13] reviewed the challenges of the cell-to-module efficiency gap and stated that the main power losses in CIGS modules with respect to CIGS solar cells are optical and caused by the front contact, typically ZnO:Al (AZO). Therefore, the application of highly transparent TCOs as front contact in CIGS modules is promising to reduce the optical losses and thus the cell-to-module efficiency gap. This will further push the development and large area applications. However, at the same time the front contact must achieve a sheet resistance of around $R_{Sq} \approx 10$ Ω Sq^{-1} for a CIGS module cell width of ≈ 5 mm to avoid an increase of the module series resistance, low fill factor and efficiency losses. In conventional modules, cells are typically interconnected in series and show a substrate configuration. Thus the front contact is deposited onto the specific CIGS layer stack. These sublayers can influence the growth of the TCO, as shown in our previous work [14]. We reported that a polycrystalline ZnO layer can promote crystalline growth of In_2O_3:H resulting in increased resistivities. In addition, the electrical properties of the TCO layer were worse on the CIGS samples than on planar glass samples. CIGS absorbers are known to show a specific surface topography, which is typically

* Corresponding author.
** Corresponding author for STEM.
E-mail addresses: darja.erfurt@helmholtz-berlin.de (D. Erfurt), Chen.Li@uantwerpen.be (C. Li).
[1] Current affiliation: Electron microscopy for Materials research (EMAT), University Antwerpen, Groenenborgerlaan 171, 2020 Antwerpen, Belgium.

https://doi.org/10.1016/j.solmat.2019.110300
Received 7 July 2019; Received in revised form 12 November 2019; Accepted 14 November 2019
Available online 29 November 2019
0927-0248/© 2019 The Authors. Published by Elsevier B.V. This is an open access article under the CC BY license (http://creativecommons.org/licenses/by/4.0/).

described by the root mean square (RMS) roughness [15–18] and can be influenced by growth conditions and treatments after deposition. The rough topography of the substrate material can therefore affect the growth and the properties of the indium oxide layers.

These results are similar to research by Keller et al. [11], which pointed out increased resistivities of In_2O_3 thin films on CIGS samples compared to reference films on planar substrates. However, Koida et al. presented mini-modules with In_2O_3:H [10] and In_2O_3:H,W [19] front contacts without losses in the electrical performance of the TCOs. Moreover, the electrical properties of the In_2O_3:H-based films were similar on planar glass and rough CIGS samples, contrary to the results by Keller et al. [11]. The reported mini-modules exhibited improved short circuit current densities and overall efficiencies compared to reference modules with ZnO:Al. The results pointed out that In_2O_3:H-based TCOs are promising front contacts for the application in large scale CIGS modules.

To improve the understanding of the impact of the substrate roughness on the indium oxide films, controlled studies are needed. This can be realized e.g. by the usage of textured glass samples and CIGS samples fabricated under different conditions. Furthermore, the influence of the deposition technique on the growth of the indium oxide films must be investigated. A deeper insight into these effects will help to develop the application of such TCOs in CIGS devices and improve the efficiency of CIGS modules in large-area applications or other devices. Moreover, such studies can help to understand similar effects in other scientific fields, where a significant dependence of thin films properties on the substrate morphology are observed. For example, also in perovskite/CIGS tandem solar cells the CIGS roughness can be critical [20].

The objective of this study is therefore to determine influences of the CIGS morphology on the properties of hydrogen doped indium oxide films and to improve the understanding of the influence of a rough substrate texture on indium oxide growth in general.

2. Experimental

2.1. Sample preparation

To investigate the influence of the CIGS roughness on the electrical properties and the structure of the indium oxide films, five sample sets were prepared. Each set has a sub-set of samples with detailed condition variations. Four sets are based on CIGS samples while the fifth is based on a textured glass substrate. Table 1 gives an overview of the set configurations and main variations.

The CIGS films were deposited by a 3-stage coevaporation process, either on bare or Mo-coated soda lime glass (SLG). Mo was deposited by magnetron sputtering. The CIGS deposition process followed three recipes, processed at Helmholtz-Zentrum Berlin für Materialien und Energie (HZB) (recipes: HZB-A, HZB-B) or National Institute of Advanced Industrial Science and Technology (AIST) (recipe: AIST). A general description of the deposition processes at HZB and AIST can be found elsewhere [21,22]. Typically "thick" CIGS films were deposited, resulting in thicknesses of ≈ 2.4 μm (HZB) and ≈ 1.9 μm (AIST), when grown on Mo-coated substrates. To grow CIGS samples with different properties and thus topography the CIGS thickness of the samples from Set 1 was adjusted by the total process and deposition time. Process times of ≈ 110 min, 71 min and 46 min resulted in CIGS average thicknesses of 2.29 μm, 1.48 μm and 0.57 μm on Mo-coated glass and 1.49 μm, 1.28 μm and 0.51 μm on bare glass substrates. The variation in CIGS thickness on Mo-coated and bare glass presumably results due to different sticking coefficients and therefore different initial growth and growth speed. The samples are referred to as "thick", "medium thick" and "thin". A post deposition treatment (PDT) with NaF or NaF/KF was applied partly for the CIGS absorbers used in Set 3. In Set 5 textured glass substrates are used, the texture was generated externally by etching [23].

Either CdS, deposited by chemical bath deposition, or Zn(O,S), deposited by radio frequency (RF) magnetron sputtering were used as buffer layer. If a highly resistive (HR) layer was applied, either intrinsic ZnO (i-ZnO) or InGaZnO (In:Ga:Zn of 1:1:1) was used, both deposited by sputtering. The deposition conditions of the Zn(O,S) films and the i-ZnO films (in combination with HZB-A CIGS samples and for Set 5) can be found elsewhere [14].

The different indium oxide layers were deposited dynamically either by in-line pulsed direct current (DC) magnetron sputtering or in-line reactive plasma deposition (RPD). For sputtering a planar In_2O_3 target was used. The deposition gases Ar, Ar-O_2 mixture and H_2O were added for deposition. The water vapor was introduced through a needle valve from a water reservoir. For the deposition of sputtered In_2O_3 films from Set 1 and 5 the following deposition conditions were used (see also [14]): a target power density of 0.8 W cm^{-2} at a total pressure of 0.31 Pa, a duty cycle of 76% with a dynamic deposition rate of 6.5 nm m min^{-1}, the base pressure before and after the introduction of water vapor was $4.6 \cdot 10^{-5}$ Pa and $8.5 \cdot 10^{-4}$ Pa, respectively. The difference approximately represents the water vapor pressure used for deposition, which is $p(H_2O) \approx 8.0 \cdot 10^{-4}$ Pa. Additionally the $p(H_2O)$ was monitored by a residual gas analyzer to be $\approx 6.8 \cdot 10^{-4}$ Pa before the process. These values are in good agreement. For comparability the first value will be used in this work. For the deposition of sputtered In_2O_3 films from Set 3 the following deposition conditions were used: a target power density of 2.7 W cm^{-2} at a total pressure of 0.4 Pa, a duty cycle of 79% with a dynamic deposition rate of 29 nm m min^{-1}, the base pressure before (after) the introduction of water vapor was $5.3 \cdot 10^{-5}$ Pa ($3.0 \cdot 10^{-3}$ Pa), thus $p(H_2O) \approx 2.9 \cdot 10^{-3}$ Pa. The residual water vapor before the intentional introduction is significantly smaller and thus negligible.

The RPD-In_2O_3:H and In_2O_3:H,W films were deposited following previous work [3]. For the RPD films of Set 3 the water vapor pressure, monitored by quadrupole mass spectrometry (Inficon Transpector XPR3), before (during) deposition was in the range of $2.9 - 4.9 \cdot 10^{-5}$ Pa ($2.0 - 2.4 \cdot 10^{-4}$ Pa), the oxygen and argon flow ratios were set to 44 and 140 ml min^{-1}, respectively. The deposition conditions of the RPD - In_2O_3:H,W films of Set 4 were varied: (i) on InGaZnO: the $p(H_2O)$ was varied and adjusted by the pumping time after venting the deposition chamber to realize relatively high (after 1 day) and low (after 3 days) $p(H_2O)$. Before (during) deposition it was $3.7 \cdot 10^{-5}$ Pa ($3.6 \cdot 10^{-4}$ Pa) and $3.2 \cdot 10^{-5}$ Pa ($8.8 \cdot 10^{-5}$ Pa), respectively. For each water vapor pressure the oxygen flows were varied: 30, 44 and 60 ml min^{-1} with a fixed dynamic deposition rate of ≈ 25 nm m min^{-1}; (ii) on i-ZnO: low $p(H_2O)$ and an oxygen flow of 44 ml min^{-1} with dynamic deposition rates of ≈ 25, 54 and 79 nm m min^{-1}. The thickness of the indium oxide films in Sets 3 and 4 is around 150 nm, in Sets 1 and 5 around 330 nm.

ZnO:Al films applied in Set 2 were deposited by magnetron sputtering and have a thickness of ≈ 865 nm. The TCO films of Sets 1 and 2 are intended to achieve sheet resistances of about 10 Ω Sq^{-1} on planar substrates. For Sets 1, 2, 5 Zn(O,S)-, Zn(O,S)/i-ZnO-, or i-ZnO coated planar glass references were used for a more accurate comparison. The reference samples for Sets 3 and 4 are blank planar glass substrates.

Selected samples were annealed. Samples from Sets 1 and 5 were annealed in vacuum at ≈ 180 °C for 60 min. Samples that are coated with In_2O_3:H,W (Set 4, $q(O_2) = 60$ ml min^{-1}) were annealed in nitrogen atmosphere at $p = 7 \cdot 10^4$ Pa at varied temperatures (150 °C - 250 °C). The dwell time of each annealing cycle was 30 min.

For the sake of simplicity, the sample stack below the TCO layer is referred to as substrate or CIGS / textured glass sample from now on.

2.2. Characterization

The morphology of the surfaces was evaluated by topographic images (20 x 20 μm^2) measured by atomic force microscopy (AFM) using a XE-70 SPM with a silicon tip (PPP-NCHR) in dynamic mode (Sets 1, 5:

Table 1
Variation of the specimen architecture within specific sample sets.

Set	Glass	Mo	CIGS		Buffer	HR-layer	TCO	Deposition
			Recipe	Thickness				
1	Planar	With, without	HZB-A[a]	Thin, medium, thick	Zn(O,S)	i-ZnO, none	In_2O_3:H	Sputtering
2	Planar	With, without	HZB-A[a]	Thick	Zn(O,S)	i-ZnO	ZnO:Al	Sputtering
3	Planar	With	HZB-B[b], AIST[c]	Thick	CdS	i-ZnO	In_2O_3:H In_2O_3:H In_2O_3:H,W	Sputtering RPD RPD
4	Planar	With	HZB-B[a]	Thick	CdS	InGaZnO, i-ZnO	In_2O_3:H,W	RPD
5	Textured	Without	Without	–	Zn(O,S)	i-ZnO, none	In_2O_3:H	Sputtering

[a]Without PDT.
[b]With and without NaF - PDT.
[c]With and without NaF,KF - PDT.

before In_2O_3:H deposition; Sets 2, 3: before HR-layer deposition). The images were analyzed with the software Gwyddion (www.gwyddion.net). The thickness of the indium oxide films was measured by spectral ellipsometry (J.A. Woolam, M-2000) in case of the RPD films or by profilometry (DektakXT by Bruker) in case of the sputtered films. The charge carrier density and electron mobility of the TCO films were determined by Hall Effect measurements in van der Pauw configuration (Toyo, ResiTest8300 or ECOPIA HMS-3000). In case of the annealed In_2O_3:H,W samples of Set 4 the Hall Effect measurements were performed after each annealing cycle. The sheet resistance/resistivity was measured in van der Pauw configuration and/or by 4 point probe (RM3-AR by Jandel). Scanning transmission electron microscopy (STEM) investigations were performed using a JEOL JEM-ARM 200CF electron microscope equipped with a cold FEG, a CEOS DCOR probe corrector, a Gatan GIF Quantum ERS electron energy-loss spectrometer (EELS), and a 100 mm^2 JEOL Centurio EDX detector. The sample was prepared by focused ion beam (FIB). Additionally the structure was evaluated by scanning electron microscopy (SEM) using a LEO Gemini 1530 with an acceleration voltage of 5 kV. The crystallinity of the indium oxide films was investigated by X-ray diffraction (XRD) in grazing incidence configuration with an angle of incidence of 2° on a Bruker D8.

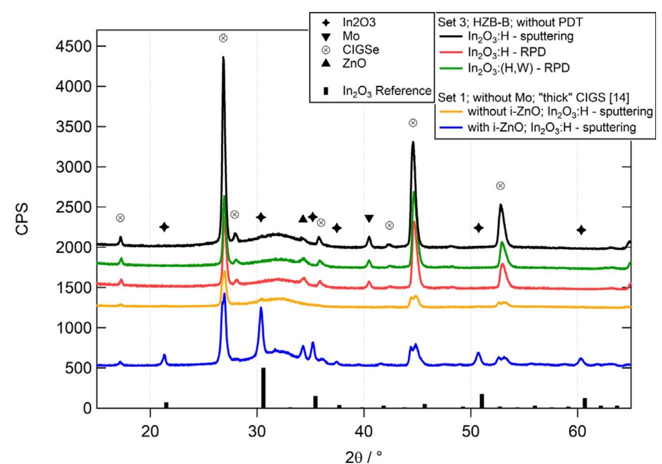

Fig. 1. XRD patterns of as-grown In_2O_3:H-based films deposited by sputtering or RPD on different samples. The patterns are shifted vertically for improved clarity. Reference pattern of In_2O_3 is taken from PDF 00-006-0416.

3. Results

3.1. TCO properties

First, the as-grown crystalline structure of the In_2O_3:H-based films is analyzed by XRD measurements on representative samples. For the characterization of sputtered In_2O_3:H films the following samples are used: (i) Set 1 without Mo on “thick” CIGS with and without i-ZnO and (ii) Set 3 with HZB-B-CIGS. The characterization of the RPD-In_2O_3:H and RPD-In_2O_3:H,W films from Set 3 is also conducted on HZB-CIGS samples. The corresponding X-ray diffraction patterns are shown in Fig. 1.

For the RPD-films no peak could be associated with the reflexes of the In_2O_3 reference pattern. Thus, the films are completely amorphous. The patterns of the sputtered In_2O_3:H films from Set 3 and from Set 1 without i-ZnO show a small peak at $2\theta \approx 30.4°$. Thus, it is concluded that the films are mainly amorphous with some crystalline nuclei. In contrast, the sputtered In_2O_3:H film from Set 1 grown on i-ZnO shows a higher peak intensity and is therefore concluded to be partly amorphous with an increased crystalline fraction, as reported in our previous work [14]. There we showed that a polycrystalline ZnO sublayer can promote the crystalline growth of sputtered In_2O_3:H films. At higher water partial pressures this effect can be minimized, as seen here for the sputtered In_2O_3:H film from Set 3, which was deposited at higher $p(H_2O)$ compared to the films from Set 1. The structures of the sputtered In_2O_3:H films from Set 1 are also representative for the In_2O_3:H films from Set 5 since the same direct sublayers were used and the In_2O_3:H films were deposited in the same sputtering run. Similar results are observed on planar samples. Note that although the monitored $p(H_2O)$ before the sputtering processes is higher than before the RPD processes, the sputtered films show a higher crystalline fraction.

For the sake of simplicity for these samples we will distinguish between three structures of the as-grown indium oxide-based films in further evaluations showing increased crystalline fractions: completely amorphous, mainly amorphous and partly amorphous.

The water vapor supplied for the deposition of the RPD layers in Set 4 generally leads to amorphous layers, as for the samples of Set 3, whereas the higher water partial pressure leads to a greater suppression of crystallite formation [3].

In the following we will present the electrical properties of first the AZO-coated samples of Set 2, second the RPD-In_2O_3:H,W-coated samples from Set 4 and third the samples from Sets 1, 3 and 5.

The ρ of the AZO thin films is 726 μΩ cm on the planar reference and 695 μΩ cm to 707 μΩ cm on the CIGS samples. The n_e and μ_e are around $3.6 \cdot 10^{20}$ cm^{-3} to $3.7 \cdot 10^{20}$ cm^{-3} and 23.1 cm^2 V^{-1} s^{-1} to 24.9 cm^2 V^{-1} s^{-1}. The electrical properties are thus very similar regardless of the used substrate.

For the samples of Set 4 we varied the deposition conditions of RPD-In_2O_3:H,W thin films grown on planar SLG and rough CIGS samples. The measured n_e, μ_e and ρ are shown in Fig. 2. Films grown on SLG at high $p(H_2O)$ typically exhibit higher n_e, but lower μ_e than films grown at low $p(H_2O)$ at a fixed oxygen flow. The increase of the oxygen flow during deposition results in a decreased n_e, i.e. from $4.2 \cdot 10^{20}$ cm^{-3} to $2.2 \cdot 10^{20}$ cm^{-3} and from $4.6 \cdot 10^{20}$ cm^{-3} to $2.9 \cdot 10^{20}$ cm^{-3} for low and high $p(H_2O)$, respectively, and in an improved μ_e for all reference films on SLG, namely from 37 cm^2 V^{-1} s^{-1} to 50 cm^2 V^{-1} s^{-1} and from 30 cm^2 V^{-1} s^{-1} to 42 cm^2 V^{-1} s^{-1} for low and high $p(H_2O)$, respectively. No clear influence due to the dynamic deposition rate is observed. The n_e of films deposited on CIGS samples was similar to films deposited on planar glass in all cases. However, the μ_e of all films grown on CIGS is limited and does not exceed 30 cm^2 V^{-1} s^{-1}. Films grown at high $p(H_2O)$ show again lower μ_e than films grown at low $p(H_2O)$, similar to the reference films. No improvement is observed with increased dynamic deposition rate. The low μ_e of films grown on CIGS leads to higher ρ than in the planar reference films.

Films which were deposited at $q(O_2) = 60$ ml min^{-1} and a dynamic deposition rate of ≈ 25 nm m min^{-1} were annealed to trigger solid phase crystallization, resulting in general in a decreased n_e and increased μ_e. However, also after annealing the films grown on rough CIGS samples showed poorer electrical properties than reference films on planar substrates. Figure S1 illustrates the change of the electrical properties of the In_2O_3:H,W thin films after several annealing cycles.

On the planar reference samples the n_e, μ_e and ρ of the as-grown indium oxide thin films of Sets 1, 3 and 5 are in the range of $3.6 \cdot 10^{20}$ cm^{-3} to $4.7 \cdot 10^{20}$ cm^{-3}, 27.7 cm^2 V^{-1} s^{-1} to 43.5 cm^2 V^{-1} s^{-1} and 374 μΩ cm to 606 μΩ cm. The influence of an increased crystalline growth of In_2O_3:H and the co-doping with W on the electrical properties of films on planar substrates is discussed elsewhere [3,14]. Compared to the planar reference samples, the indium oxide films grown on CIGS samples show slightly lower n_e, decreased μ_e and thus increased ρ, actually by factors of 1.10 to 4.33. These values were confirmed by two methods, as shown in Figure S2. Besides, the ρ of films grown on textured glass samples increased by factors of 1.05 to 1.19. As will be shown in Section 3.3 one key aspects of these wide variations are the different types of samples and their topography, which therefore will be investigated in more detail to explain its influence on the electrical properties of the indium oxide films.

3.2. Topological analysis of the substrates

The substrate topography of the CIGS samples was varied by the recipe and the process duration and investigated by AFM. As an example Fig. 3 shows topographic images of three specimen before TCO deposition, each with an indicated profile line from which the shown height profile and the profile of the local slope are taken. Note that the slope profile is taken from the corresponding local slope map. The three specimen are: (a) a "thin" CIGS sample from Set 1 without a Mo-layer, (b) a "thick" CIGS sample from Set 1 with a Mo-layer and (c) a textured glass sample from Set 5. The RMS roughness values of the samples are 40 nm, 118 nm and 175 nm, respectively. Compared to the rather smooth CIGS sample the rough CIGS sample shows higher peak-to-valley distances with higher slopes at the edges of the features. The textured glass sample shows larger features and profile heights. However, the transitions between the features are rather smooth. To further describe the topography we introduced additional parameters. From the local slope map we determined the median local slope (MLS) of the samples. Using the Watershed method [24] we estimate the median equivalent square size of the marked features. This value is used to describe the median feature size (MFS). To minimize the influence of noise, only marked areas with a threshold over 20 px^2 are considered. An example for the analytic routine is shown in Figure S3 in the supplemental information. In Fig. 3 the RMS and MLS values of the samples are included. Due to the large features appearing on the textured glass the local slope values show less fluctuation, as especially the slope changes preferably at the edges of the specific features. Thus, not only the slope but also its alternating sequence has to be taken into account for an improved characterization of the surface features. We therefore calculated the ratio of the median local slope and the median feature size (MLS/MFS). For the samples shown in Fig. 3 the highest (lowest) value will thus result for the rather rough CIGS (textured glass) sample. Table 2 presents the characteristic topographic values RMS,

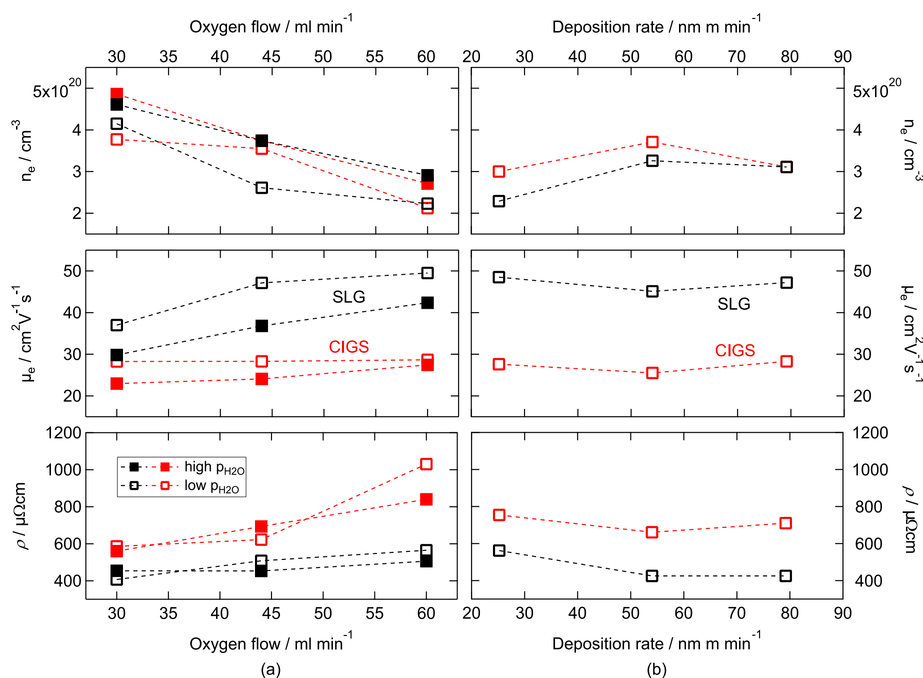

Fig. 2. Comparison of the charge carrier density, electron mobility and resistivity of as-grown In_2O_3:H,W thin films on planar SLG and CIGS samples in dependence of (a) the deposition conditions water vapor pressure and oxygen flow with a deposition rate of ≈ 25 nm m min^{-1}, InGaZnO as the HR-layer and (b) the varied deposition rate at low $p(H_2O)$, $q(O_2)$ of 44 ml min^{-1} and i-ZnO as the HR-layer.

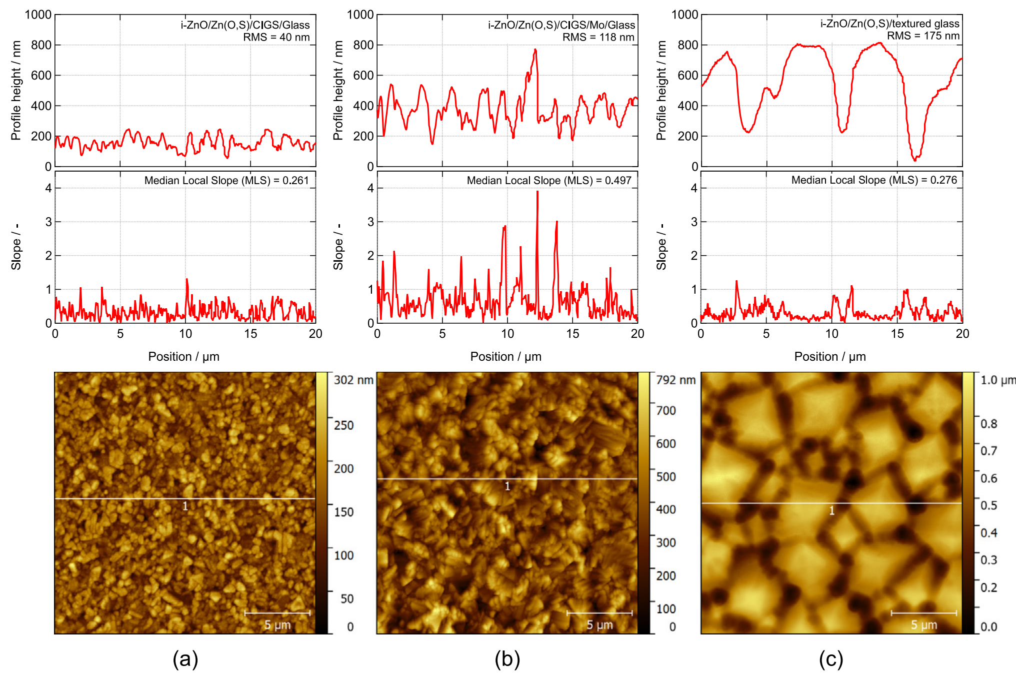

Fig. 3. Profile height, local slope and corresponding AFM topography images with profile line of (a) a rather smooth CIGS sample, (b) a rather rough CIGS sample and (c) a textured glass sample before In_2O_3:H deposition; the local slope profile was obtained from the corresponding local slope map.

Table 2
Roughness parameter of the varied sample configurations: RMS roughness, MLS, MFS and MLS/MFS.

Set	Glass	Mo	CIGS/PDT	RMS /nm	MLS –	MFS /μm^2	MLS/MFS /μm^{-2}
1	Planar	With	HZB-A: thin	27	0.172	0.166	1.03
			HZB-A: medium	89	0.371	0.170	2.18
			HZB-A: thick	118	0.497	0.185	2.69
		Without	HZB-A: thin	40	0.261	0.150	1.74
			HZB-A: medium	55	0.331	0.153	2.17
			HZB-A: thick	65	0.385	0.148	2.60
2	Planar	With	HZB-A: thick	113	0.495	0.187	2.64
		Without	HZB-A: thick	59	0.410	0.198	2.07
3	Planar	With	HZB-B: no PDT	87	0.477	0.165	2.89
			HZB-B: NaF	80	0.466	0.163	2.86
			AIST: no PDT	38	0.282	0.189	1.49
			AIST: NaF, KF	52	0.341	0.183	1.86
5	Textured	Without	–	175	0.276	1.329	0.21
–	Planar	–	–	0.3	0.004	0.15	0.03

MLS, MFS and MLS/MFS of the substrates from Sets 1, 2, 3, and 5. The CIGS samples used for Set 4 were not characterized specifically by AFM, because their topography is most likely similar to the HZB-B CIGS samples without PDT from Set 3, since the same deposition recipe was used. The values of a blank planar glass substrate are added for reference. For all samples no significant effect from the layers between the TCO and CIGS on the roughness is expected.

The reduction of the CIGS deposition time within Set 1 led to a reduced CIGS film thickness, RMS roughness and MLS. The drop of the RMS and MLS values is more pronounced for films deposited on glass/Mo than on bare glass and correlates typically with the total CIGS thickness. The MFS of the CIGS samples grown on bare glass is lower than that of films grown on Mo-coated glass.

The post deposition treatments had no clear influence on the topography. While the NaF-treated HZB samples are smoother, the NaF & KF-treated AIST samples are rougher than the corresponding non-treated reference sample.

The variations for Set 3 revealed that the "thick" samples prepared at HZB have higher RMS and MLS values than samples prepared at AIST, the estimated MFS is slightly smaller. The textured glass sample of Set 5 has a much higher RMS and MFS values compared to the CIGS samples. However, the median local slope is as low as in rather smooth CIGS samples. The RMS roughness of the blank planar glass substrate is two to three, the MLS two orders of magnitude smaller than of the remaining samples. For reasons of comparability the same routine of the MFS determination was applied as for the other samples.

The results show that the morphology of the substrates vary significantly. In the following section we will analyze its impact on the electrical properties of the different TCOs.

3.3. Correlation of the properties of the TCO and the substrates' topography

3.3.1. Electrical properties

As described above, the electrical properties of TCOs vary due to different TCO deposition methods and conditions. To compare the change of the n_e, μ_e and ρ of the studied films among each other, the values on the rough samples are normalized to the corresponding value on the planar reference sample. Fig. 4 illustrates their change

in dependence on the (a) RMS roughness and (b) MLS/MFS. Shown are the samples from Sets 1, 2, 3 and 5 after deposition. The electrical properties are indexed as effective (eff), because the thickness is not constant owing to the different slopes. This can have an significant impact on the Hall Effect measurement results [25]. The measured values are shown in Figure S4 in the supplemental information, here also the values of the annealed samples from Set 1 are included.

Compared to the planar references the effective charge carrier density ($n_{e,\mathrm{eff}}$) of indium oxide films grown on CIGS samples is on average 10% lower. No clear influence of the substrate's morphology is evident. However, the $n_{e,\mathrm{eff}}$ of the partly amorphous grown sputtered In_2O_3:H films seems to decrease with increased roughness. The effective electron mobility ($\mu_{e,\mathrm{eff}}$) of the films drops systematically by up to 60% with increase in either RMS or MLS/MFS and is the main origin for the rise of the effective resistivity (ρ_{eff}). The drop in $\mu_{e,\mathrm{eff}}$ is more pronounced for the sputtered films than for films deposited by RPD and will be discussed later. According to these findings a pronounced loss in $\mu_{e,\mathrm{eff}}$ is expected also for films deposited on textured glass samples, which have the highest RMS value. Surprisingly, almost no losses are observed.

This effect can be better explained by the relatively small MLS/MFS value, which is similar to the value of planar glass. This indicates that not the substrate profile heights and peak-to-valley-values, but the slope and its alternating sequence are more detrimental for the effective electron mobility.

From Fig. 4 it becomes evident that the slopes of the $\mu_{e,\mathrm{eff}}$-loss differ for the indium oxide film in dependence on their deposition conditions. Thus, there must be another effect in addition to the influence of the substrate topography. The drop in $\mu_{e,\mathrm{eff}}$ is more pronounced with increase in crystalline fraction of the indium oxide based films after deposition. The completely amorphous grown RPD films show the shallowest slope, which becomes steeper for the mainly amorphous grown sputtered films and even more steep for the partly amorphous grown sputtered films. Among the RPD films the In_2O_3:H,W films show slightly higher $\mu_{e,\mathrm{eff}}$ than the In_2O_3:H films. However, as the gap between the corresponding values is very small the difference is regarded as not meaningful although a beneficial effect of the co-doping with tungsten cannot be excluded completely.

Consequently, there are two important influencing variables which result in a degraded electron mobility of hydrogen doped indium oxide films on rough substrates: (i) the local slope at the surface and its alternating rate and (ii) the crystalline fraction after deposition.

Contrary to the findings in case of the indium oxide-based TCOs no influence of the CIGS topography on the electrical properties of ZnO:Al is observed.

3.3.2. Structural properties

To investigate the limiting effect on the electron mobility and the structure of the indium oxide films STEM measurements were carried out on a CIGS sample with RMS = 87 nm and a sputtered as-grown In_2O_3:H top layer from Set 3. Fig. 5 presents two characteristic regions, in which crack-shaped voids are indicated by red arrows. In Fig. 5(a) two voids in the In_2O_3:H layer with a width of ≈ 15 nm can be clearly observed. Fig. 5(b) presents another void with a width of ≈ 5 nm, which

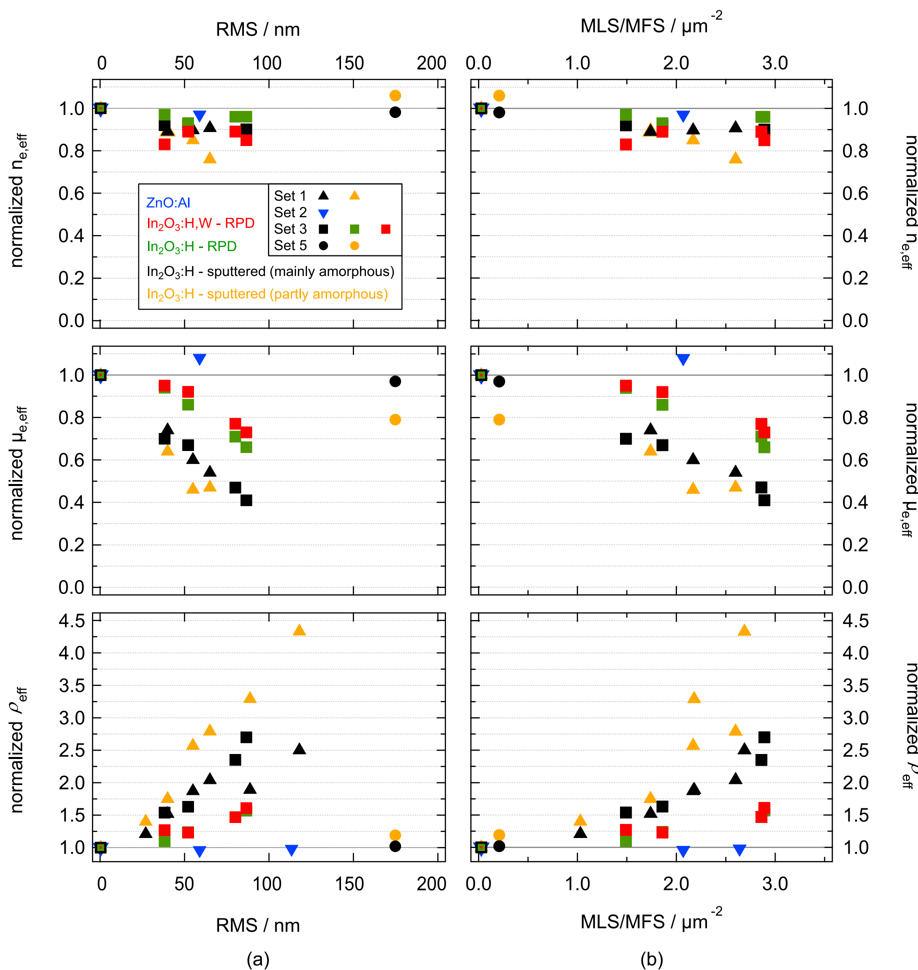

Fig. 4. Change of the effective charge carrier density ($n_{e,\mathrm{eff}}$), effective electron mobility ($\mu_{e,\mathrm{eff}}$) and effective resistivity (ρ_{eff}) of as-grown In_2O_3:H and In_2O_3:H,W films in dependence on the corresponding (a) RMS roughness and (b) MLS/MFS of the different substrates used; the values are normalized to the planar reference samples.

forms in the In_2O_3:H layer, close to the ZnO interface. Moreover, it can be seen that the voids form at triangle-shaped valleys, which can be considered as a sharp transition in surface morphology. Over a width of 17 μm more than 10 voids were observed. In general, the majority of the voids could be aligned with CIGS grain boundaries (GBs). Figure S5 presents images of the elemental compositions of the region shown in Fig. 5(a), measured by EELS. Within the area of the voids no indium or other material is detected, confirming the void structure. The STEM measurements additionally reveal that the CdS lattice follows the lattice of CIGS with many twins and defects. Furthermore, some coherent lattice relationship between ZnO and CdS is observed. In contrast, no such relationship is found for In_2O_3:H and i-ZnO. Corresponding images are shown in Figure S6 in the supplemental information.

The structure of as-grown In_2O_3:H films is further evaluated by cross-section SEM measurements to compare their structure on different film-stacks. In Fig. 6 five SEM images are shown: two samples from Set 1: (a) glass/CIGS/Zn(O,S)/i-ZnO/In_2O_3:H (RMS = 40 nm) and (b) glass/Mo/CIGS/Zn(O,S)/i-ZnO/In_2O_3:H (RMS = 118 nm); two samples from Set 3 (RMS = 87 nm): glass/Mo/HZB-CIGS/CdS/i-ZnO with (c) sputtered-In_2O_3:H or (d) RPD-In_2O_3:H; one sample from Set 5 (RMS = 175 nm): (e) textured glass/Zn(O,S)/i-ZnO/In_2O_3:H. The In_2O_3:H layer grown on the textured glass sample seems to cover the whole surface without void formation. In contrast the In_2O_3:H films grown on CIGS samples seem to be disconnected in some areas. These areas are indicated by red arrows and are assumed to be voids, as found by STEM investigation. Their amount and size increase with increased CIGS RMS roughness and MLS/MFS, respectively, as can be seen from Fig. 6(a) and (b). The In_2O_3:H films in Fig. 6(c) and (d) look more homogeneous, although also here areas in the films can be observed, which may be voids.

4. Discussion

The results show that the electrical properties of the In_2O_3:H-based TCOs change tremendously when grown by sputtering or RPD on rough samples, such as CIGS, instead of planar substrates. The conductivity is limited by the electron mobility, most likely due to the formation of voids inside the indium oxide films at high local slopes at the substrate surface, e.g. above CIGS GBs. STEM measurements of such a sample confirm the morphology of high local slopes at ridges and V-shaped valleys at the CIGS surface with the TCO layers following the same morphology. Moreover, the STEM images clearly show that the voids begin their formation at the V-shaped valleys of the CIGS surface. These valleys are located at the boarders of the CIGS GBs. The V-shaped valleys on the CIGS surface can be explained by the Zener pinning effect, which has been reported in other oxide materials [26]. According to the Zener pinning effect, the GBs attract defects and vacancies during growth of polycrystalline materials, which in turn favors the growth of pores and voids along the GBs. In comparison to the areas in the grain interior, the growth of GBs is "pinned" and dragged along by the propagating reaction interface, hence the V-shaped topography forms always at the end of GBs. This also explains the columnar shape of CIGS grains and the doming morphology on the CIGS surface. When CdS and ZnO layers are grown on the surface of CIGS, two effects occur. On the one hand the doming morphology leads to lower deposition rates of the sputtered or evaporated materials due to simple geometric shadowing. On the other hand, since CdS and ZnO growth follows the lattice of CIGS grains, the same Zener pinning effect happens for CdS and ZnO. The hydrogen-doped indium oxide layers grown on the CIGS sample surface show typically an amorphous structure, therefore the shading effect dominates. All these lead to more and more void collection at the V-shaped valleys at the TCO layer, where the large voids were always found. The results demonstrate that a specific amount of sharp ridges and valleys result in a defined amount of voids in the TCO layer, which are likely to act as barriers for electrons and prevent current flow. Moreover, this is confirmed by the fact that the effective electron mobility does not decrease when the indium oxide films are deposited on substrates with high RMS roughness but low MLS/MFS values, i.e. here textured glass samples.

A specific amount of voids limits the effective electron mobility to a certain value, as observed for In_2O_3:H,W deposited at several conditions on CIGS samples with RMS roughnesses of ≈ 87 nm. As shown in Fig. 2(a) the measured μ_e was limited at ≈ 30 $cm^2\ V^{-1}\ s^{-1}$, although the electron mobility of the reference films could be improved due to variations in deposition conditions. As the same type of CIGS samples is used, we assume that the amount of voids within the In_2O_3:H,W films on CIGS is also very similar. However, the quality of the In_2O_3:H,W material between the voids is assumed to be as good as in the reference films. The local μ_e of these parts is therefore presumably higher than determined by Hall Effect measurements over a comparatively wide distance. Due to the combination of voids and material in the lateral direction, the films are considered to be inhomogeneous and thus the electrical properties are denoted as effective, as mentioned above.

Previous work from other groups has raised up the hypotheses of the importance of voids. For instance Keller et al. [11] reported a higher sheet resistance for sputtered In_2O_3:H films when grown on CIGS samples and assumed voids to be the origin. The work of Jäger et al. [27] indicates voids in sputtered In_2O_3:H films on CIGS samples, too. Our experiments confirm the existence of voids and their negative effect for the electron mobility.

In addition to the described morphological effect we found that an increased crystalline fraction of the as-grown hydrogenated indium oxide films affects the electron mobility of the films and leads to a more pronounced drop at a defined roughness. The increased crystalline fraction in combination with a still high amount of amorphous phase may prevent merging of the material at voids and thus support the

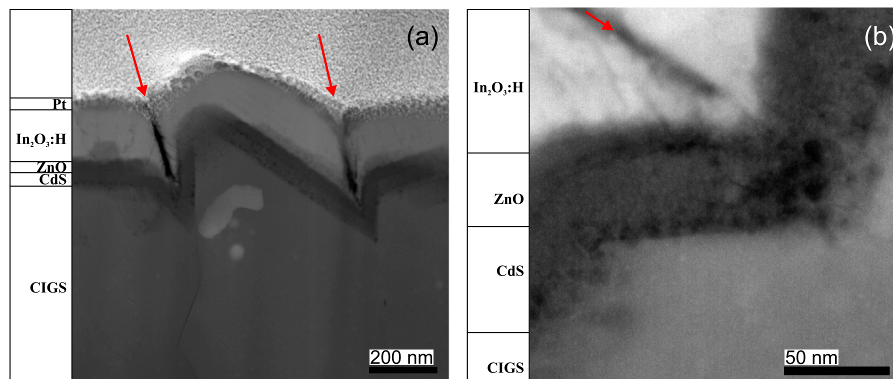

Fig. 5. STEM images (a), (b) of as-grown sputtered In_2O_3:H films grown on i-ZnO/CdS/CIGS with a RMS value of 87 nm and a MLS/MFS of 2.9 μm^{-2} after CdS deposition; voids are clearly visible in the In_2O_3:H layer (crack-like dark areas indicated by red arrows).

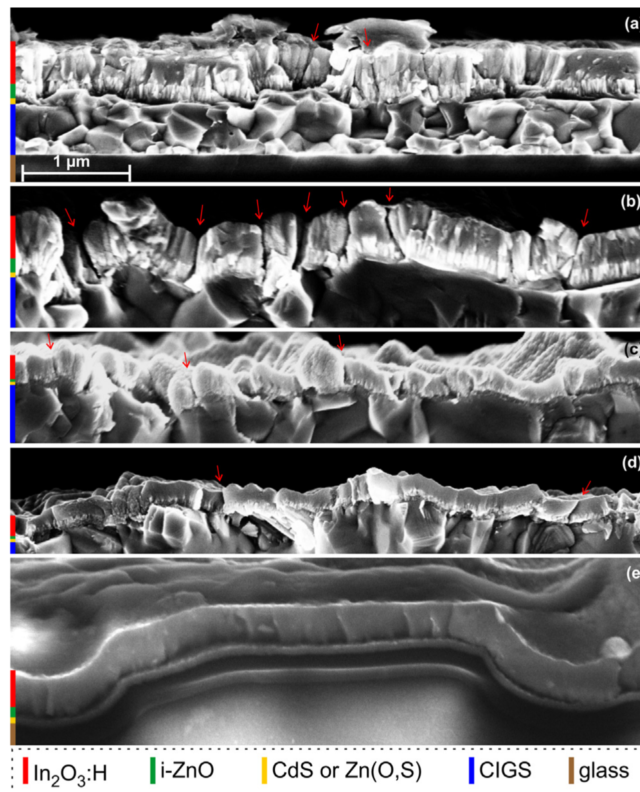

Fig. 6. SEM images of as-grown In_2O_3:H films from Set 1: (a) glass/CIGS/Zn(O,S)/i-ZnO/In_2O_3:H (RMS = 40 nm) and (b) glass/Mo/CIGS/Zn(O,S)/i-ZnO/In_2O_3:H (RMS = 118 nm); from Set 3 (RMS = 87 nm): glass/Mo/HZB-CIGS/CdS/i-ZnO with (c) sputtered-In_2O_3:H or (d) RPD-In_2O_3:H; from Set 5 (RMS = 175 nm): (e) textured glass/Zn(O,S)/i-ZnO/In_2O_3:H; all images are taken with the same magnification, colored boxes on the left side of each image illustrate the different materials in cross-section; areas in which voids are presumed are indicated by a red arrow.

ongoing propagation of these features. Note that the width of the voids is constant along a relatively wide film thickness.

In contrast, the sputtered ZnO:Al thin films, which are known to grow crystalline [28–31], show no increase in resistivity and no drop in electron mobility when grown on CIGS samples. We assume that the crystalline ZnO:Al films, even though some voids might form, coalesce at very low thicknesses and do thusly not affect the electrical properties. In fact, Greiner et al. [32] showed that ZnO:Al films grow irregular at the edges of tranches, but do not affect the electrical properties of the as-grown ZnO:Al films. However, these structures must be considered regarding the electrical stability, as shown by damp heat tests [32].

From the literature it is known that the nuclei density is lower in films grown by RPD than in films grown by magnetron sputtering [3]. Moreover, the energy of the deposited particles is suggested in the literature as a significant difference between the two techniques. In RPD it is less than 40 eV during In_2O_3:Sn deposition. Contrary, in sputtering methods particles such as backscattered argon and negative oxygen ions are supposed to have high energies above 100 eV. The lower energies and higher ionization rates of the depositing particles are considered to be the origin of the higher quality of the RPD films, i.e. In_2O_3:Sn [33]. This may be an additional reason for the higher effective electron mobilities found in the RPD films compared to the sputtered indium oxide films.

However, because the effective electron mobility of the indium oxide films is still low after solid phase crystallization, we assume that the voids do not coalesce at all or not sufficiently during the thermal treatment. Thus, the effective electron mobility of the indium oxide films deposited on rough CIGS samples has to be improved already in the as-grown condition to minimize the deficit. However, this is a topic of further research.

The most important benefit of In_2O_3:H and In_2O_3:H,W films after solid phase crystallization is in general the outstanding trade-off between optical and electrical properties compared to conventionally used TCOs such as ZnO:Al. Therefore, these materials are considered to be a promising front contact in CIGS modules. Typically the TCO sheet resistance is in the range of 10 Ω Sq^{-1}. However, when the CIGS samples have a rough topography with high RMS and MLS/MFS values, the sheet resistance of the hydrogenated indium oxide films will be significantly higher on CIGS than required. Consequently the module series resistance and fill factor will be affected, limiting the module efficiencies. Thus, for a successful application of In_2O_3:H-based TCOs in CIGS modules the topography of the CIGS samples is of high importance. This might also concern other fields of applications where rough substrates are used. The required TCO sheet resistance may still be achieved by the use of smooth CIGS samples and/or the adjustment of the TCO thickness. However, the latter will lead to an increase in parasitic absorption and therefore reduce the possible gain in short circuit current density.

5. Conclusion

Hydrogen doped and hydrogen-tungsten co-doped indium oxide thin films were deposited on planar and textured glass samples as well as on CIGS samples with different topographies by sputtering or reactive plasma deposition. Two important factors are found which affect the electron mobility of In_2O_3:H-based films grown on rough samples: (i) Typically at the surface close to CIGS grain boundaries high sloped ridges and V-shaped valleys are observed. Such structures cause crack-shaped void formation inside the In_2O_3:H-based films, which act as an electron barrier, prevent current flow and thus limit the effective electron mobility over a comparatively wide lateral distance. Considering only CIGS samples, the drop of the effective electron mobility can be well described by the RMS value. To compare substrates with very different topography types we introduced a new

parameter, the ratio of the median local slope to the median feature size (MLS/MFS), determined by AFM. We show that this parameter can be more suitable to describe the losses. (ii) The effective electron mobility of In_2O_3:H-based films grown on CIGS samples drops more pronounced with increase in crystalline fraction after deposition. But even the completely amorphous In_2O_3:H-based films showed poorer electron mobilities when grown on rough CIGS samples.

The effective electron mobility does not improve by changing the deposition conditions such as water vapor pressure, oxygen supply or deposition rate, as shown for In_2O_3:H,W thin films. Although solid phase crystallization of the amorphous films improved the electron mobility in general, it does not lead to sufficient reduction of the deficit in comparison to the planar reference samples. To overcome this deficit in the electrical properties of the indium oxide films on rough CIGS it is therefore necessary to improve the effective electron mobility of the films already before annealing by avoiding and/or reducing void formation. This is topic of further research. In total the use of completely amorphous grown In_2O_3:H-based films in combination with a thermal treatment to trigger solid phase crystallization and usage of smooth samples (low MLS/MFS) is most suitable and promising for the application in CIGS modules or other devices with rough topographies to avoid electrical losses and increased series resistance.

Declaration of competing interest

The authors declare that they have no known competing financial interests or personal relationships that could have appeared to influence the work reported in this paper.

CRediT authorship contribution statement

Darja Erfurt: Conceptualization, Methodology, Investigation, Writing - original draft, Visualization. **Takashi Koida:** Investigation, Resources, Writing - review & editing, Supervision. **Marc D. Heinemann:** Conceptualization, Resources, Supervision, Project administration. **Chen Li:** Investigation, Writing - review & editing, Visualization. **Tobias Bertram:** Resources, Writing - review & editing. **Jiro Nishinaga:** Resources. **Bernd Szyszka:** Supervision. **Hajime Shibata:** Supervision. **Reiner Klenk:** Conceptualization, Writing - review & editing, Supervision. **Rutger Schlatmann:** Supervision, Funding acquisition.

Acknowledgments

This work was supported by the German Federal Ministry for Economic Affairs and Energy under contract number 0325762G (TCO4CIGS). The authors thank M. Hartig, K. Mayer-Stillrich, I. Dorbandt, B. Bunn, M. Kirsch for technical support. C. Li is grateful for financial support from Max Planck Society, Germany and technical support from the MPI FKF StEM group members.

Appendix A. Supplementary data

Supplementary material related to this article can be found online at https://doi.org/10.1016/j.solmat.2019.110300.

References

[1] T. Koida, H. Fujiwara, M. Kondo, Hydrogen-doped In_2O_3 as high-mobility transparent conductive oxide, Japan. J. Appl. Phys. 46 (2007) L685–L687, http://dx.doi.org/10.1143/JJAP.46.L685.

[2] H. Scherg-Kurmes, S. Körner, S. Ring, M. Klaus, L. Korte, F. Ruske, R. Schlatmann, B. Rech, B. Szyszka, High mobility In_2O_3:h as contact layer for a-Si:H/c-Si heterojunction and μc-Si:H thin film solar cells, Thin Solid Films 594 (2015) 316–322, http://dx.doi.org/10.1016/j.tsf.2015.03.022.

[3] T. Koida, Y. Ueno, H. Shibata, In_2O_3-based transparent conducting oxide films with high electron mobility fabricated at low process temperatures, Phys. Status Solidi (a) 215 (2018) 1700506, http://dx.doi.org/10.1002/pssa.201700506.

[4] F. Meng, J. Shi, Z. Liu, Y. Cui, Z. Lu, Z. Feng, High mobility transparent conductive W-doped In_2O_3 thin films prepared at low substrate temperature and its application to solar cells, Sol. Energy Mater. Sol. Cells 122 (2014) 70–74, http://dx.doi.org/10.1016/j.solmat.2013.11.030.

[5] E. Kobayashi, Y. Watabe, T. Yamamoto, High-mobility transparent conductive thin films of cerium-doped hydrogenated indium oxide, Appl. Phys. Express 8 (2015) 015505, http://dx.doi.org/10.7567/APEX.8.015505.

[6] M. Morales-Masis, E. Rucavado, R. Monnard, L. Barraud, J. Holovsky, M. Despeisse, M. Boccard, C. Ballif, Highly conductive and broadband transparent Zr-doped In_2O_3 as front electrode for solar cells, IEEE J. Photovolt. 8 (2018) 1202–1207, http://dx.doi.org/10.1109/JPHOTOV.2018.2851306.

[7] A.E. Delahoy, S.Y. Guo, Transparent and semitransparent conducting film deposition by reactive-environment, hollow cathode sputtering, J. Vac. Sci. Technol. A 23 (2005) 1215–1220, http://dx.doi.org/10.1116/1.1894423.

[8] T. Koida, H. Fujiwara, M. Kondo, High-mobility hydrogen-doped In_2O_3 transparent conductive oxide for a-Si:H/c-Si heterojunction solar cells, Sol. Energy Mater. Sol. Cells 93 (2009) 851–854, http://dx.doi.org/10.1016/j.solmat.2008.09.047.

[9] L. Barraud, Z. Holman, N. Badel, P. Reiss, A. Descoeudres, C. Battaglia, S. De Wolf, C. Ballif, Hydrogen-doped indium oxide/indium tin oxide bilayers for high-efficiency silicon heterojunction solar cells, Sol. Energy Mater. Sol. Cells 115 (2013) 151–156, http://dx.doi.org/10.1016/j.solmat.2013.03.024.

[10] T. Koida, Y. Ueno, J. Nishinaga, H. Higuchi, H. Takahashi, M. Iioka, H. Shibata, S. Niki, Cu(in, ga)se_2 solar cells with amorphous in_2o_3-based front contact layers, ACS Applied Materials & Interfaces 9 (2017) 29677–29686, http://dx.doi.org/10.1021/acsami.7b07092.

[11] J. Keller, A. Aijaz, F. Gustavsson, T. Kubart, L. Stolt, M. Edoff, T. Törndahl, Direct comparison of atomic layer deposition and sputtering of In_2O_3:H used as transparent conductive oxide layer in $CuIn_{1-x}Ga_xSe_2$ thin film solar cells, Sol. Energy Mater. Sol. Cells 157 (2016) 757–764, http://dx.doi.org/10.1016/j.solmat.2016.07.012.

[12] M. Nakamura, K. Yamaguchi, Y. Kimoto, Y. Yasaki, T. Kato, H. Sugimoto, Cd-Free Cu(in, Ga)(Se, S)$_2$ Thin-Film Solar Cell with a New World Recordefficacy of 2335%, 6th IEEE PVSC, Chicago, IL, June 19, 2019, 2019, see also http://www.solar-frontier.com/eng/news/2019/0117_press.html, (Online; Accessed 24May2019).

[13] V. Bermudez, A. Perez-Rodriguez, Understanding the cell-to-module efficiency gap in Cu(In, Ga)(S, Se)$_2$ photovoltaics scale-up, Nat. Energy 3 (2018) 466–475, http://dx.doi.org/10.1038/s41560-018-0177-1.

[14] D. Erfurt, M.D. Heinemann, S.S. Schmidt, S. Körner, B. Szyszka, R. Klenk, R. Schlatmann, Influence of ZnO-based sub-layers on the growth of hydrogen doped indium oxide, ACS Appl. Energy Mater. 1 (2018) 5490–5499, http://dx.doi.org/10.1021/acsaem.8b01039.

[15] M. Bouttemy, P. Tran-Van, I. Gerard, T. Hildebrandt, A. Causier, J. Pelouard, G. Dagher, Z. Jehl, N. Naghavi, G. Voorwinden, B. Dimmler, M. Powalla, J. Guillemoles, D. Lincot, A. Etcheberry, Thinning of CIGS solar cells: Part I: Chemical processing in acidic bromine solutions, Thin Solid Films 519 (2011) 7207–7211, http://dx.doi.org/10.1016/j.tsf.2010.12.219.

[16] Z. Jehl, F. Erfurth, N. Naghavi, L. Lombez, I. Gerard, M. Bouttemy, P. Tran-Van, A. Etcheberry, G. Voorwinden, B. Dimmler, W. Wischmann, M. Powalla, J. Guillemoles, D. Lincot, Thinning of CIGS solar cells: Part II: Cell characterizations, Thin Solid Films 519 (2011) 7212–7215, http://dx.doi.org/10.1016/j.tsf.2010.12.224.

[17] T. Mise, T. Nakada, Microstructural properties of $(In, Ga)_2Se_3$ precursor layers for efficient CIGS thin-film solar cells, Sol. Energy Mater. Sol. Cells 93 (2009) 1000–1003, http://dx.doi.org/10.1016/j.solmat.2008.11.028.

[18] V. Deprédurand, T. Bertram, M. Thevenin, N. Valle, J.-N. Audinot, S. Siebentritt, Alternative etching for improved Cu-rich $CuInSe_2$ solar cells, MRS Proc. 1771 (2015) 163–168, http://dx.doi.org/10.1557/opl.2015.447.

[19] T. Koida, Y. Ueno, J. Nishinaga, Y. Kamikawa, H. Higuchi, M. Iioka, H. Takahashi, H. Shibata, S. Niki, Current status of transparent conducting oxide layers with high electron mobility and their application in Cu(In, Ga)Se_2 minimodules, Thin Solid Films 673 (2019) 26–33, http://dx.doi.org/10.1016/j.tsf.2019.01.024.

[20] Q. Han, Y.-T. Hsieh, L. Meng, J.-L. Wu, P. Sun, E.-P. Yao, S.-Y. Chang, S.-H. Bae, T. Kato, V. Bermudez, Y. Yang, High-performance perovskite/cu(in, ga)se2 monolithic tandem solar cells, Science 361 (6405) (2018) 904–908, http://dx.doi.org/10.1126/science.aat5055.

[21] T. Kodalle, M.D. Heinemann, D. Greiner, H.A. Yetkin, M. Klupsch, C. Li, P.A. van Aken, I. Lauermann, R. Schlatmann, C.A. Kaufmann, Elucidating the mechanism of an RbF post deposition treatment in CIGS thin film solar cells, Solar RRL 2 (2018) 1800156, http://dx.doi.org/10.1002/solr.201800156.

[22] T. Koida, J. Nishinaga, Y. Ueno, H. Higuchi, H. Takahashi, M. Iioka, H. Shibata, S. Niki, Impact of front contact layers on performance of Cu(In, Ga)Se_2 solar cells in relaxed and metastable states, Prog. Photovolt., Res. Appl. 26 (2018) 789–799, http://dx.doi.org/10.1002/pip.3017.

[23] S. Neubert, S. Ring, F. Welker, S. Götzendörfer, F. Ruske, B. Stannowski, R. Schlatmann, B. Rech, Very thin, highly-conductive ZnO:Al front electrode on textured glass as substrate for thin-film silicon solar cells, Phys. Status Solidi (RRL) – Rapid Research Letters 8 (2014) 44–47, http://dx.doi.org/10.1002/pssr.201308195.

[24] P. Klapetek, I. Ohlí dal, D. Franta, A. Montaigneand-Ramil, A. Bonanni, D. Stifter, H. Sitter, Atomic force microscopy characterization of znte epitaxial films, Acta Physica Slovaca 53 (2003).

[25] G.H. Blount, R.H. Bube, A.L. Robinson, Interpretation of equilibrium and steady state hall and thermoelectric effects in inhomogeneous materials, J. Appl. Phys. 41 (1970) 2190–2195, http://dx.doi.org/10.1063/1.1659188.

[26] C. Li, T. Griffiths, T.J. Pennycook, C. Mangler, P. Jeřábek, J. Meyer, G. Habler, R. Abart, The structure of a propagating $MgAl_2O_4$/MgO interface: linked atomic- and μm-scale mechanisms of interface motion, Phil. Mag. 96 (2016) 2488–2503, http://dx.doi.org/10.1080/14786435.2016.1205233.

[27] T. Jäger, Y.E. Romanyuk, S. Nishiwaki, B. Bissig, F. Pianezzi, P. Fuchs, C. Gretener, M. Döbeli, A.N. Tiwari, Hydrogenated indium oxide window layers for high-efficiency Cu(In, Ga)Se_2 solar cells, J. Appl. Phys. 117 (2015) 205301, http://dx.doi.org/10.1063/1.4921445.

[28] W. Yang, Z. Liu, D.-L. Peng, F. Zhang, H. Huang, Y. Xie, Z. Wu, Room-temperature deposition of transparent conducting Al-doped ZnO films by RF magnetron sputtering method, Appl. Surf. Sci. 255 (2009) 5669–5673, http://dx.doi.org/10.1016/j.apsusc.2008.12.021.

[29] W. Yang, Z. Wu, Z. Liu, A. Pang, Y.-L. Tu, Z.C. Feng, Room temperature deposition of Al-doped ZnO films on quartz substrates by radio-frequency magnetron sputtering and effects of thermal annealing, Thin Solid Films 519 (2010) 31–36, http://dx.doi.org/10.1016/j.tsf.2010.07.048.

[30] K.H. Kim, K.C. Park, D.Y. Ma, Structural, electrical and optical properties of aluminum doped zinc oxide films prepared by radio frequency magnetron sputtering, J. Appl. Phys. 81 (1997) 7764–7772, http://dx.doi.org/10.1063/1.365556.

[31] T. Koida, T. Kaneko, H. Shibata, Carrier compensation induced by thermal annealing in Al-doped ZnO films, Materials 10 (2017) 141, http://dx.doi.org/10.3390/ma10020141.

[32] D. Greiner, S. Gledhill, C. Köble, J. Krammer, R. Klenk, Damp heat stability of Al-doped zinc oxide films on smooth and rough substrates, Thin Solid Films 520 (2011) 1285–1290, http://dx.doi.org/10.1016/j.tsf.2011.04.190.

[33] H. Kitami, M. Miyashita, T. Sakemi, Y. Aoki, T. Kato, Quantitative analysis of ionization rates of depositing particles in reactive plasma deposition using mass-energy analyzer and Langmuir probe, Japan. J. Appl. Phys. 54 (2015) 01AB05, http://dx.doi.org/10.7567/JJAP.54.01AB05.